Nonradiative recombination in strongly interacting silicon nanocrystals embedded in amorphous silicon-oxide films

Jeremy A. Rowlette,[1,2,*] Rohan D. Kekatpure,[1,3] Matt A. Panzer,[2] Mark L. Brongersma,[3] and Kenneth E. Goodson[2]
[1]*Department of Electrical Engineering, Stanford University, Stanford, California 94305, USA*
[2]*Department of Mechanical Engineering, Stanford University, Stanford, California 94305, USA*
[3]*Department of Materials Science and Engineering, Stanford University, Stanford, California 94305, USA*
(Received 27 May 2009; published 16 July 2009)

The optically induced free-carrier absorption coefficient (α_{FC}) of densely packed (2×10^{18} cm^{-3}) Si nanocrystals (NCs) embedded in a glass matrix was accurately measured in the near-infrared using two complementary pump-probe techniques. When compared to established carrier dynamical models, the dependence of α_{FC} on optical pump intensity reveals enhanced nonradiative recombination at high pump intensity (>10 KW/cm^2), which can be explained by the interaction of excited carriers located in spatially separated NCs. The rate of recombination due to the interaction between a pair of excited NCs is determined to increase inversely with the sixth power of their separation distance ($\tau^{-1}\sim\gamma R^{-6}$; $\gamma\approx2.6\times10^{-31}$ cm^6 s^{-1}) and is indicative of near-field dipole-dipole energy transfer. These results explain the source of an apparent inconsistency in power-law behavior found in previous carrier dynamics studies on similar materials which did not account for this interaction.

DOI: 10.1103/PhysRevB.80.045314 PACS number(s): 78.67.Bf, 72.20.Jv, 72.40.+w, 78.30.Am

I. INTRODUCTION

Si nanocrystals (NCs) formed inside of a host dielectric film exhibit strong and stable room-temperature visible and near-infrared luminescence[1–8] as well as the ability to efficiently sensitize codoped Er^{3+} atoms emitting near 1540 nm.[9,10] These properties offer potential pathways to achieving practical Si-based coherent light sources thus making these materials of great technological interest. In addition, the fundamental physics of efficient light emission in low-dimensional semiconductors having indirect band gaps as well as the dynamics of closely packed interacting quantum dots (QDs) or NCs are rapidly advancing fields of study which continue to provide intriguing questions of fundamental importance.

Despite great interest in their optical properties, it has been well-established that free-carrier absorption (FCA) and fast nonradiative carrier recombination (NRCR), such as Auger processes, severely limit the net optical gain in Si NC-dielectric films to impractical levels.[1,4,11–13] Progress toward fully understanding these intrinsic loss mechanisms which compete unfavorably with stimulated emission has been impeded by the substantial size inhomogeneity that is characteristic of most common forms of these films, e.g., porous Si (PS),[5,6] Si-rich Si oxides (SRO) (Refs. 1–4) and nitrides (SRN),[8] making it difficult to disentangle the effects of competing optoelectronic phenomena.[14,15] Our limited understanding of NRCR and FCA losses in PS and SRO films is evident by the establishment of multiple seemingly contradicting sets of carrier rate equations over the past two decades, cf. Refs. 6, 13, and 16–18. In order to reconcile these differences, we have precisely measured the optically induced FCA losses of dense SRO films over an extended pump intensity range and have compared the results to existing carrier dynamical models. We find that none of the existing rate equation models is capable of accurately reproducing the pump intensity dependence over the full range of data. However, by introducing a single near-field Coulombic dipole-dipole interaction term of similar form as described in Ref. 19 between excited NCs to the independent (i.e., noninteracting) NC coupled rate equation model by Kovalev *et al.*,[16] we are able to accurately reproduce the data over the full range of pump intensities. Furthermore, we find that the existing rate equation models can be interpreted as limiting forms of this model.

II. EXPERIMENTAL METHODS AND RESULTS

Samples were prepared by depositing thin films of SRO on either fused-silica or Si substrates using a plasma-enhanced chemical-vapor deposition process followed by a 1 h 1100 °C anneal in a pure N_2 ambient.[13] High-resolution TEM imaging shows crystalline Si precipitates which were determined to have a lognormal size distribution with mean diameter of 5.4 nm and a concentration of 2×10^{18} cm^{-3}.[4,13] The FCA coefficient (α_{FC}) was measured as a function of pump intensity using two complementary pump-probe methods which are schematically represented in Fig. 1. Both data sets are plotted in Fig. 2 on a logarithmic scale to emphasize the power-law dependence of α_{FC} on pump intensity. Data set A was obtained by monitoring the loss-induced spectral broadening of the 895 nm photoluminescence (PL) line of a pedestal supported microdisk resonator with a 500-nm-thick SRO active region. The details of this experimental setup can also be found in Ref. 13. The pump beam was the 488 nm line of a CW Ar-ion laser and was incident normal to the top of the disk. The probe beam was the resonant PL emission itself. Data set B was obtained by measuring the steady-state (negative time-delay) component of transient differential absorption (TDA) measurements performed with pump and probe beams of wavelength 532 nm and 1064 nm, respectively, and were both generated from the same mode-locked Nd:YVO_4 laser (9 ps FWHM pulse and 82 MHz repetition frequency). The beams were collinear and normally incident to the sample consisting of a blanket 500-nm-thick SRO film fabricated on a transparent fused-silica substrate. The pump

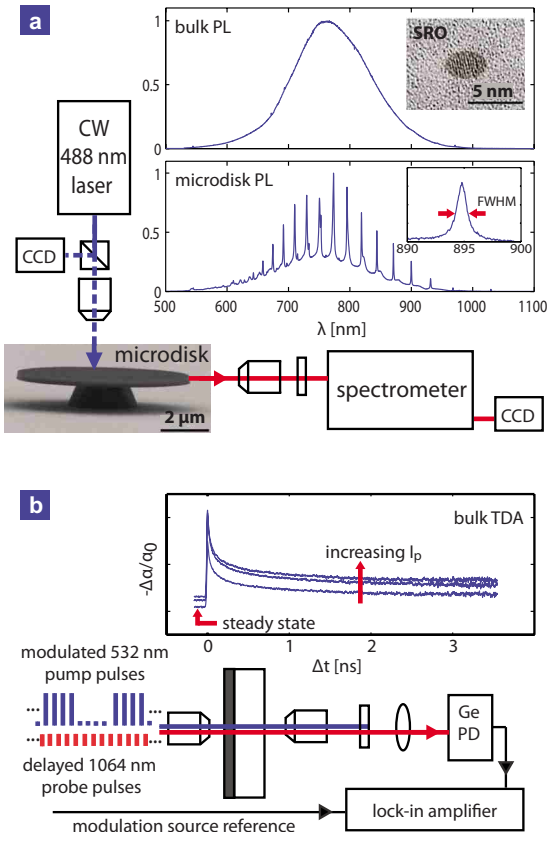

FIG. 1. (Color online) Two experimental methods used to determine the optically induced FCA losses in SRO films by measuring the (a) loss-induced spectral broadening of the 895 nm PL emission line of an SRO microdisk resonator and the (b) steady-state (negative time-delay) component of picosecond TDA measurements performed on a 500-nm-thick SRO film deposited on a fused-silica substrate.

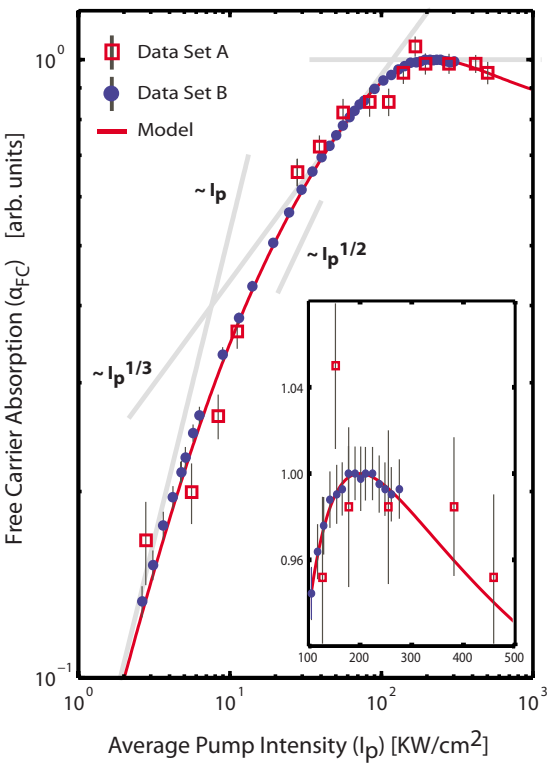

FIG. 2. (Color online) The normalized free-carrier absorption coefficient ($\alpha_{FC}/\max\{\sigma_{FC}\}$ and $\max\{\alpha_{FC}\}=24.6\pm0.3$ cm^{-1} at 1064 nm) vs pump intensity for the two complementary pump-probe measurement techniques described in the text and in Fig. 1. The solid red curve is the best fit for the proposed model. Linear, 1/3 and 1/2 power-law curves are included as visual guides. The inset is a zoomed in view of the maximum at 200 KW/cm^2.

beam was externally modulated by an electro-optic modulator with a 100 KHz square wave and passed through a second-harmonic generator to produce 532 nm light. A lock-in amplifier was used to isolate the magnitude of the probe signal at the fundamental modulation frequency and was normalized by the time-averaged detected probe signal. Despite the two very different experimental techniques used, both data sets are in perfect agreement to within the precision of the measurements. Intensities below 1 KW/cm^2 and above 500 KW/cm^2 were not accessible due to either low SNR or limitations in pump beam-spot size, respectively. The data were highly repeatable on multiple samples prepared during different fabrication runs and we observed no hysteresis in any of the data.

α_{FC} transitions from an approximate 1/2 power law ($\sim I_p^{0.58}$) to an exact 1/3 power law (between 30 and 80 KW/cm^2) before saturating between 100 and 200 KW/cm^2 and then declining above a maximum value of 24.6 ± 0.3 cm^{-1} ($\sigma_{FC}\approx1.2\times10^{-17}$ cm^{-2}) at 200 KW/cm^2. The pump photon energies (2.54 and 2.33 eV) fall within the absorption band of the SRO films[4,13] where the dominant loss mechanism is through the generation of electron-hole pairs (EHPs). In contrast, the probe photon energies (1.39 and 1.17 eV) lie far outside of the absorption band of the SRO film.[4,13] Thus, probe absorption is negligible in the absence of pump excitation. Increased absorption of the probe beam upon photoexcitation by the pump at an energy sufficient to generate EHPs, combined with the absence of hysteresis, are characteristics consistent with optically induced FCA.

III. MODELING

Charge densities exhibiting 1/2 and 1/3 power-law dependences on pump intensity are characteristics of bulk semiconductors owing to two (e.g., bimolecular Auger[6]) and three-particle Auger processes,[20] respectively. Therefore, given the observed power-law behavior of the data, bulklike linear-plus-quadratic[6,17,18] or linear-plus-cubic[13] loss rate models could explain the data below 10 and 100 KW/cm^2, respectively. However, these models do not predict saturation at high intensities, which is a key signature of isolated or independent NCs.[16,21] The independent NC model by Kovalev *et al.*[16] provides the closest fit to the data but, in its current form, cannot reproduce the data to within experimental uncertainty. Motivated by the observation of the 1/3 power-law behavior, we modify the isolated NC model[16] to include a single cubic interaction term between NCs resulting in the following set of coupled rate equations:

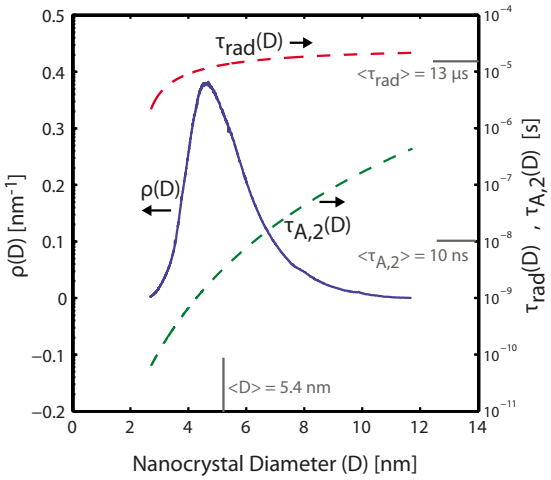

FIG. 3. (Color online) Physical properties of the SRO films measured in this work. τ_{rad} was obtained from transient PL experiments described in Ref. 4 and $\tau_{A,2}$ was computed using the formula, $\tau_{A,2}^{-1}=C_{\mathrm{A}}(2/V)^2$, with $C_{\mathrm{A}}=4\times10^{-31}$ cm^6/s and $V=(\pi/6)D^3$. The distribution function was calculated using the methodology described in Refs. 4 and 13.

$$\dot{N}_0 = -\phi\sigma_{01}N_0 + N_1/\tau_1 + \Gamma N^{*2}N_1, \tag{1a}$$

$$\dot{N}_1 = \phi\sigma_{01}N_0 - \phi\sigma_{12}N_1 - N_1/\tau_1 + N_2/\tau_{A,2} - \Gamma N^{*2}N_1, \tag{1b}$$

$$\dot{N}_2 = \phi\sigma_{12}N_1 - N_2/\tau_{A,2}, \tag{1c}$$

$$N_T = N_0 + N_1 + N_2, \tag{1d}$$

where $N_T(D)$ and $N_j(D,t)$ are the densities of NCs with diameter D and those having j EHPs, respectively, ϕ is the instantaneous pump photon flux, σ_{ij} is the absorption cross section for promoting a NC from the ith to the jth e-h state, τ_1 is the single EHP recombination lifetime including both radiative (rad) and nonradiative (nrad) channels, ($\tau_1^{-1}=\tau_{\mathrm{rad}}^{-1}+\tau_{\mathrm{nrad}}^{-1}$), and $\tau_{A,2}$ is the two EHP Auger recombination lifetime. Higher excitation levels [$\mathbf{O}(N_3)$] have been omitted because their steady-state occupations are deemed to be negligible for all measured intensities. For the same considerations, we neglect interactions between NCs of higher excitation levels than those which are in the N_1 state and write the cubic interaction term as the product of N_1 and $(N^*)^2$. Here, we have defined N^* as the instantaneous average concentration of NCs containing one EHP, i.e., $N^*(t)\equiv\int\rho(D)N_1(t,D)dD$, where $\rho(D)$ is the unit normalized distribution of NC diameters which we have plotted in Fig. 3.[4,13] We interpret the physical meaning of this interaction as an increase in the nonradiative decay of a selected NC in the N_1 state due to the presence of neighboring NCs also in the N_1 state, whose strength increases in proportion to $\langle\langle N_1\rangle\rangle^2$ or inversely to the sixth power of their average separation distance, i.e., $\tau^{-1}\sim\langle\langle R_1\rangle\rangle^{-6}$, where $\langle\langle R_1\rangle\rangle\sim\langle\langle N_1\rangle\rangle^{-1/3}$.[22] Such a dependence is indicative of near-field Coulombic dipole-dipole coupling.[19] However, unlike the case explicitly treated in Ref. 19, where an EHP in one NC interacts with the ground state of a neighboring NC, here the interaction occurs between two EHPs located in separated NCs in close proximity to each other. Such a resonant nonradiative energy-transfer mechanism was first investigated by Fröhlich and Mahr[23] for a system of excited F centers in KI crystals.

By treating each parameter as a constant[24] and setting $\sigma_{ij}=\sigma$ for all i and j, we obtain an analytical steady-state expression for $\langle\langle N_1\rangle\rangle$ and $\langle\langle N_2\rangle\rangle$

$$\Gamma\langle\langle N_1\rangle\rangle^3 + [\phi\sigma + \phi^2\sigma^2\tau_{A,2} + 1/\tau_1]\langle\langle N_1\rangle\rangle - \phi\sigma\langle\langle N_T\rangle\rangle = 0, \tag{2a}$$

$$\langle\langle N_2\rangle\rangle = \phi\sigma\tau_{A,2}\langle\langle N_1\rangle\rangle, \tag{2b}$$

where $\langle\langle N_1\rangle\rangle$ is found by taking the positive real root of Eq. (2a) and $\langle\langle N_T\rangle\rangle$ is the density of all NCs. The effective FCA coefficient for the entire NC system can be written as

$$\alpha_{\mathrm{FC}} = \sigma_{\mathrm{FC}}[\langle\langle N_1\rangle\rangle + e_{21}\langle\langle N_2\rangle\rangle + e_{31}\langle\langle N_3\rangle\rangle\cdots], \tag{3}$$

where e_{j1} is a dimensionless weighting coefficient which indicates the contribution of the jth EHP state to σ_{FC} relative to that of the one EHP state. Typically, the assumption $e_{j1}=j$ is made, a direct extension of the linear FCA theory for nondegenerate bulk material.[25] However, recent calculations for CdSe QDs have cast doubt on the general validity of this assumption for low-dimensional systems.[26] As we will show, we find that e_{21} must drop below unity in the steady-state case in order to reproduce the maximum observed in the data.

IV. DISCUSSION

The solid red curves in Figs. 2, 4, 5, and 6(b) are the best fits to the data using Eqs. (2) and (3) and the following optimal parameters: $\sigma=(3.84\pm0.19)\times10^{-16}$ cm^2; $\tau_1=37.72\pm1.89$ ns; $\tau_{A,2}=5.94\pm2.61$ ns; $\Gamma=(2.88\pm1.76)\times10^{-29}$ cm^6 s^{-1}; and $e_{21}=0.5\pm0.06$. Figure 4 plots the values of $\langle\langle N_1\rangle\rangle$ and $e_{21}\langle\langle N_2\rangle\rangle$ normalized by the NC density, $\langle\langle N_T\rangle\rangle$, and shows their individual contributions according to the model. The model is capable of fitting the data exceptionally well with the optimal parameter set yielding an average relative error magnitude of 0.4% and a peak error of 2.5% occurring at the lowest measured intensity. The sensitivity of the model to Γ and e_{21} is conveyed in Figs. 4(a) and 4(b), respectively. Before discussing these results in greater detail, we first demonstrate the effectiveness of the proposed analytical model over that of the independent NC model[16] in reproducing the experimental data. In Fig. 5, we compare the best fits to the data using the independent NC model[16] with values of $e_{21}=2$ (model Ia) and $e_{21}<1$ (model Ib) to that of the proposed model which includes both a reduced e_{21} and the near-field coupling term. Each model variant was optimized to minimize the root-mean-square error and no further improvements were possible through continued variation in the parameter set. As Fig. 5(b) shows, both models Ia and Ib with optimized parameters oscillate about the experimental data trend and have peak error magnitudes which substantially deviate outside of the bounds of experimental uncer-

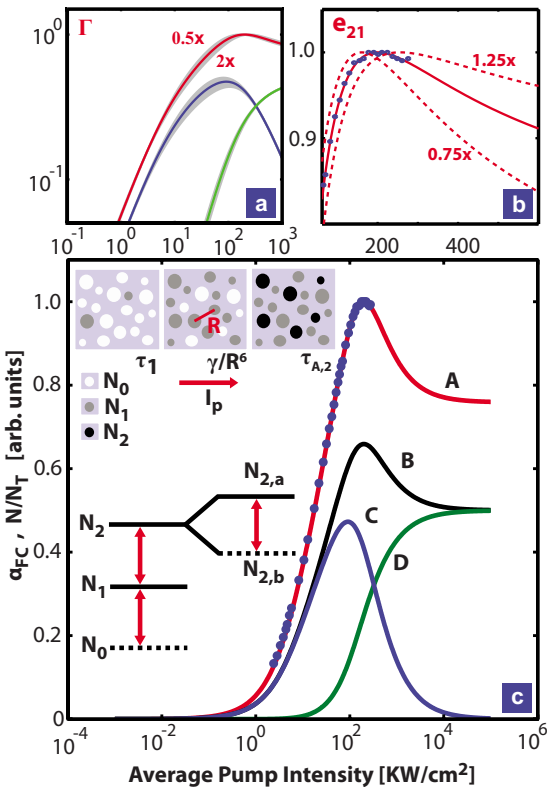

FIG. 4. (Color online) [(a) and (b)] Visualization of model sensitivity to Γ and e_{21} (c) data set B (solid circles), $N_1+e_{21}N_2$ (solid red curve labeled A) scaled to unity and (solid black curve labeled B) normalized by N_T, (solid blue curve labeled C) N_1/N_T, and (solid green curve labeled D) $e_{21}N_2/N_T$. The sequence of pictures in (c) depicts the dominant nonradiative recombination channels vs pump intensity (I_p) and the solid and dashed lines in the manifold indicate active and inactive FCA states, respectively.

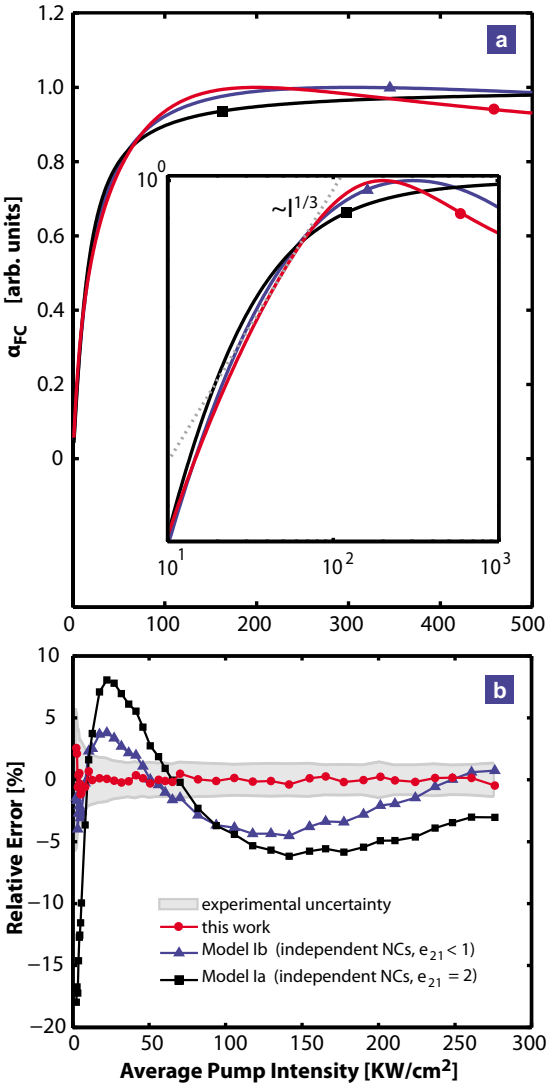

FIG. 5. (Color online) (a) Comparison of the three model variants including the independent (i.e., noninteracting) NC model (Ref. 16) with values of $e_{21}=2$ and $e_{21}<1$ (black and blue solid curves with square and triangle symbols, respectively) and the proposed model which includes near-field interaction between N_1 states (red solid curve). Each model variant is optimal with respect to fitting the data. The curves in the inset are plotted on a logarithmic scale zoomed into the region where the 1/3 power-law region is observed. (b) Relative error for the three model variants compared to the experimental uncertainty (shaded region).

tainty. For reference, the optical parameters we extract from all three model variants are tabulated in Table I.

It is instructive to compare the extracted parameter values to diameter-weighted average values using the distribution function shown in Fig. 3 obtained using the methods described in Ref. 13. For the proposed model, we find σ to be $\approx$2 times higher than the expected value of $\langle\sigma\rangle=1.71\times10^{-16}$ cm^2 obtained from transient PL measurements but is well within the accepted range of values for annealed SRO materials.[16] Furthermore, assuming the relation $\tau_{A,2}^{-1}=C_A(2/V)^2$ holds,[27] where $V=(\pi/6)D^3$ and taking $C_A=4\times10^{-31}$ cm^6/s,[28] we find $\langle\tau_{A,2}\rangle=10.26$ ns, which is also within about a factor of 2 of the value we extract. Despite the good agreement for σ and $\tau_{A,2}$, τ_1 is found to be $\approx$350 times lower than the average radiative lifetime, $\langle\tau_{rad}\rangle=13.2$ μs.[4] It is important to note that this value of τ_1 which we extract is not particularly sensitive to the model used because τ_1 primarily impacts data fitting in the low-intensity regime where existing models are in agreement. We attribute the reduced value of τ_1 to the large fraction of nrad NCs which are sampled by the pump-probe method but which are not sampled directly in PL measurements. The PL quantum efficiency (PLQE), a good measure of the fraction of rad NCs, was recently reported by Dal Negro *et al.*[8] for PL optimized SRO films exhibiting nearly identical optical properties as the films measured in this work to be about 5%. A low PLQE supports the conclusion that the pump-probe methods used in this work primarily sample the nrad-NC population. The fact that the value of σ is of similar magnitude for both rad NCs and nrad NCs suggests that localized defect states near the band edge are responsible for the reduced value of τ_1.

To gain further insight into the near-field coupling physics, we rigorously solved Eqs. (1) and (3) using Monte Carlo (MC) methods under steady-state pump conditions for a NC population having a uniform probability density of 2×10^{18} cm^{-3}. The near-field coupling between two NCs in the N_1 state located a distance R_1 apart was modeled using a

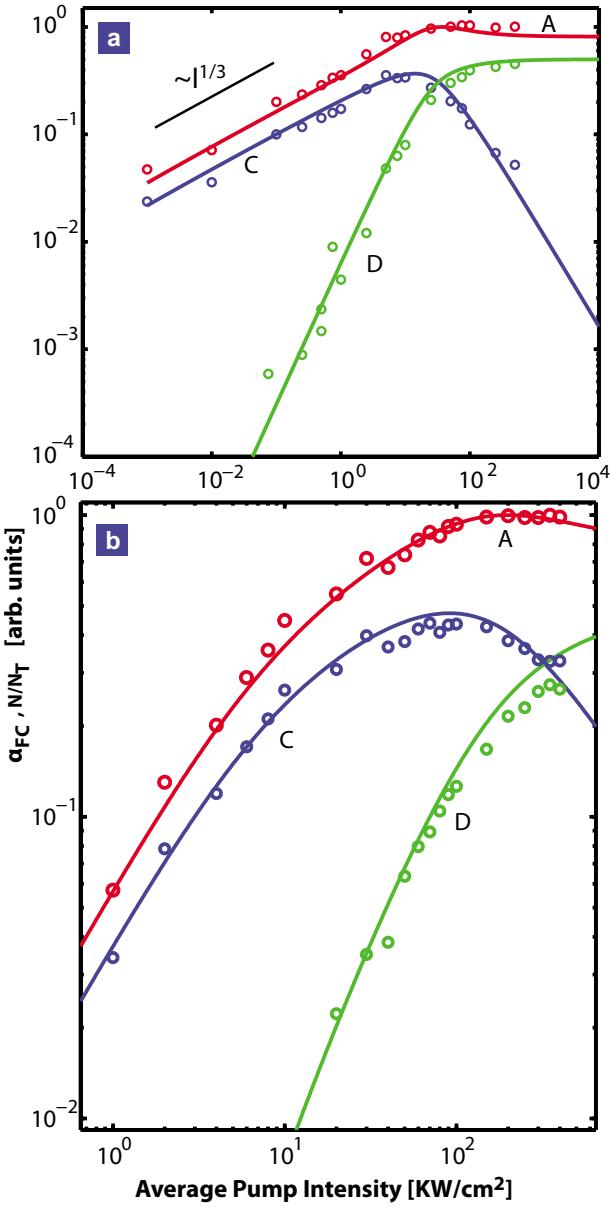

FIG. 6. (Color online) Results of MC simulations (open circles) which treat the near-field coupling between NCs in the N_1 state by a term of the form γR_1^{-6}, where R_1 is the distance between the two interacting NCs. The MC results are compared to the steady-state analytical model [Eqs. (2) and (3)] where the near-field interaction is described by $\Gamma \cdot N_1^2$ (solid curves labeled A, C, and D as defined in Fig. 4). (a) Results of MC simulation calibration performed to fine tune the ratio γ/Γ and also to demonstrate the physical equivalence of $\gamma \cdot R_1^{-6}$ and $\Gamma \cdot N_1^2$. To assist the calibration process, the material parameters were intentionally skewed ($\sigma = 3.8 \times 10^{-16}$ cm^2; $\tau_1 = 380$ μs; $\tau_{A,2} = 59$ ns; $\Gamma = 2.3 \times 10^{-29}$ cm^6 s^{-1}; and $e_{21} = 0.5$) in order to force the near-field coupling to dominate the recombination physics, and thereby exaggerate the 1/3 power-law region over an extended range of pump intensities. From the calibration, we find $\gamma/\Gamma \approx 1/110$. (b) MC simulation results using the calibrated value of $\gamma \approx \Gamma/110$ and the optimal parameter set described in the text ($\sigma = 3.8 \times 10^{-16}$ cm^2; $\tau_1 = 38$ ns; $\tau_{A,2} = 5.9$ ns; $\Gamma = 2.9 \times 10^{-29}$ cm^6 s^{-1}; and $e_{21} = 0.5$). The analytical curve is the same as in Figs. 2, 4, and 5 and accurately reproduces the experimental data.

term of the form $\tau^{-1} \sim \gamma R_1^{-6}$, where γ was the only adjustable material parameter. We calibrated the value of γ by matching the results of MC simulations to the results of the steady-state analytical model [Eqs. (2) and (3)] for a given value of Γ. To assist in the calibration of γ and to demonstrate the physical equivalence of the two forms of the near-field coupling terms (i.e., $\gamma \cdot R_1^{-6} \leftrightarrow \Gamma \cdot N_1^2$) under steady-state conditions, we selected material parameters which forced the near-field term to dominate the recombination physics over an extended range of pump intensities. A comparison of the MC calibration simulations to the analytical model with the skewed parameter set are shown in Fig. 6(a) where the 1/3 power-law region arising from the near-field interaction term is clearly visible over four orders of magnitude. A value of $\gamma \approx \Gamma/110$ was found to accurately reproduce the analytical results. The scaling factor (1/110) is entirely accounted for by integrating the near-field contribution of all neighboring NCs in the N_1 state acting on a randomly selected NC also in the N_1 state. After calibrating the value of γ, we performed MC simulations using the optimal parameter set values which provided the best fit to the data using the analytical model. The results of these simulations are shown in Fig. 6(b) along with the analytical model which was already shown to accurately fit the experimental data. Through the MC simulations, we are able to extract the effective pair interaction strength between two NCs in the N_1 state to be $\gamma \approx \Gamma/110 = (2.62 \pm 1.60) \times 10^{-31}$ cm^6/s. This value is nearly identical to the bulk Auger coefficient for silicon[20,28] and supports the conclusion that the microscopic near-field mechanism is Auger recombination involving two EHPs located in separate NCs.

To the best of our knowledge, the maximum in α_{FC} has never been reported before. It is best explained by allowing $e_{21} < 1$, i.e., N_2 states have a lower contribution to σ_{FC} relative to the N_1 states. For, if $e_{21} \geq 1$, then the α_{FC} cannot decrease because of the reaction $N_1 V + \text{photon} \rightarrow (N_1 V - 1) + (N_2 V + 1)$, where V is a unit volume, which leads to $\Delta\alpha_{FC} \sim |\Delta N_1|(e_{21} - 1) < 0$. Hence, $e_{21} < 1$ is necessary to produce a maximum, generally. However, this view conflicts with observed picosecond TDA data which have shown that FCA losses *increase* shortly after pump excitation under conditions when the fraction of newly created N_2 states should be substantial.[28] These conflicting observations suggest that e_{21} is time dependent, e.g., $e_{21}(t_0) = 2 \rightarrow e_{21}(t_\infty) = 0.5$. This could occur if the N_2 states are composed of multiple 2 e-h pair states, one group contributing to FCA ($N_{2,a}$) and the remaining group being inactive ($N_{2,b}$) or diminished, perhaps mediated by a localized or bound state.

V. CONCLUSION

In summary, inclusion of the Coulombic near-field interaction term in the isolated NC rate equations[16] reproduces the exact power-law behavior exhibited by the data, including the approximate 1/2 power-law region, which is actually a transition region between the linear and 1/3 power-law regimes. This transition results from the near-field energy transfer between excited NCs, which can be interpreted as an extended Auger recombination event between two NCs and is likely to be the source for the differences in power law

TABLE I. Comparison of extracted parameter values for the three model variations plotted in Fig. 5.

Model	e_{21}	σ ($\times 10^{-16}$ cm^2)	τ_{A2} (ns)	τ_1 (ns)	Γ ($\times 10^{-29}$ cm^6/s)
Ia	2.0	3.7	49	85	NA
Ib	0.5	1.4	1.5	122	NA
This work	0.5	3.8	5.9	37	2.9

reported.[6,13,16–18] At low excitation intensities, when the average occupancy of a NC is negligible, NCs behave as though they are isolated and α_{FC} increases linearly with pump intensity. Tunneling mediated diffusion between NCs can occur in this regime[29] but should not strongly impact FCA since σ_{FC} is not seen to be a strong function of NC size.[13] When occupancy becomes appreciable ($\approx$0.1 EHP per NC), interaction between neighboring excited NCs by means of near-field energy exchange begins to dominate over the linear radiative and nonradiative N_1 recombination. In this regime, the power-law transitions from linear to 1/3 crossing through a region that is an approximate 1/2 power law. When $N_1/N_T \approx N_2/N_T \approx 0.4$, occurring around 100 KW/cm^2, the two EHP Auger recombination channel dominates leading to saturation as predicted by the isolated NC model.[16] The exact mechanism for the reduction in the FCA at high pump intensities needs to be investigated further but the possibility of reduced losses at high-pumping conditions opens the intriguing possibility of lowered gain thresholds in lasers and amplifiers constructed from these materials.

ACKNOWLEDGMENTS

J.A.R. and M.A.P. were supported by the Semiconductor Research Corporation (Task 1640) and through the MARCO Interconnect Focus Center. R.D.K. and M.L.B. were supported by a Si-based Laser Initiative of the Multidisciplinary University Research Initiative (MURI) under the Air Force Aerospace Research (Award No. FA9550-06-1-0470) and the MARCO Interconnect Focus Center. A Department of Defense DURIP equipment grant (Award No. N00014-06-1-0496) provided funds for some of the equipment used in this work.

*Corresponding author; rowlette@stanford.edu

[1] L. Pavesi, L. Dal Negro, C. Mazzoleni, G. Franzò, and F. Priolo, Nature **408**, 440 (2000).
[2] M.L. Brongersma, P. Kik, A. Polman, K. Min, and H. Atwater, Appl. Phys. Lett. **76**, 351 (2000).
[3] R. J. Walters, J. Kalkman, A. Polman, H. A. Atwater, and M. J. A. de Dood, Phys. Rev. B **73**, 132302 (2006).
[4] R. D. Kekatpure and M.L. Brongersma, Phys. Rev. A **78**, 023829 (2008).
[5] M. V. Wolkin, J. Jorne, P. M. Fauchet, G. Allan, and C. Delerue, Phys. Rev. Lett. **82**, 197 (1999).
[6] P. Malý, F. Trojánek, J. Kudrna, A. Hospodková, S. Banáš, V. Kohlová, J. Valenta, and I. Pelant, Phys. Rev. B **54**, 7929 (1996).
[7] K. Cho, N. Park, T. Kim, K. Kim, G. Sung, and J. Shin, Appl. Phys. Lett. **86**, 071909 (2005).
[8] L. Dal Negro, J. Yi, L. Kimerling, S. Hamel, A. Williamson, and G. Galli, Appl. Phys. Lett. **88**, 233109 (2006).
[9] P. Kik, M.L. Brongersma, and A. Polman, Appl. Phys. Lett. **76**, 2325 (2000).
[10] L. Kimerling, L. Dal Negro, M. Stolfi, J. Yi, J. Michel, X. Duan, E. Sargent, T. Chang, V. Sukhovatkin, J. Haavisto, and J. LeBlanc, *Device Applications of Silicon Nanocrystals and Nanostructures* (Springer, New York, USA, 2009).
[11] P. Kik and A. Polman, J. Appl. Phys. **91**, 534 (2002).
[12] L. Dal Negro, M. Cazzanelli, N. Daldosso, Z. Gaburro, L. Pavesi, F. Priolo, D. Pacifici, G. Franzò, and F. Lacona, Physica E **16**, 297 (2003).
[13] R. Kekatpure and M.L. Brongersma, Nano Lett. **8**, 3787 (2008).
[14] V. I. Klimov, Ch. J. Schwarz, D. W. McBranch, and C. W. White, Appl. Phys. Lett. **73**, 2603 (1998).
[15] M. Sykora, L. Mangolini, R. D. Schaller, U. Kortshagen, D. Jurbergs, and V. I. Klimov, Phys. Rev. Lett. **100**, 067401 (2008).
[16] D. Kovalev, J. Diener, H. Heckler, G. Polisski, N. Künzner, and F. Koch, Phys. Rev. B **61**, 4485 (2000).
[17] D. Navarro-Urrios, A. Pitanti, N. Daldosso, F. Gourbilleau, R. Rizk, G. Pucker, and L. Pavesi, Appl. Phys. Lett. **92**, 051101 (2008).
[18] M. Yamaguchi, K. Katayama, Q. Shen, T. Toyoda, and T. Sawada, Chem. Phys. Lett. **427**, 192 (2006).
[19] G. Allan and C. Delerue, Phys. Rev. B **75**, 195311 (2007).
[20] D. B. Laks, G. F. Neumark, A. Hangleiter, and S. T. Pantelides, Phys. Rev. Lett. **61**, 1229 (1988).
[21] V. Klimov, Annu. Rev. Phys. Chem. **58**, 635 (2007).
[22] The notation $\langle\langle x \rangle\rangle$ is to be taken as the steady-state ensemble average of x.
[23] D. Fröhlich and H. Mahr, Phys. Rev. **148**, 868 (1966).
[24] Explicitly, we make the following substitutions and approximations: $\sigma \equiv \langle\langle \sigma' N_T \rangle\rangle / \langle\langle N_T \rangle\rangle \approx \langle\langle \sigma' N_1 \rangle\rangle / \langle\langle N_1 \rangle\rangle$; $\tau_{A,2} \equiv \langle\langle \tau'_{A,2} N_1 \rangle\rangle / \langle\langle N_1 \rangle\rangle$; $\tau_1^{-1} \equiv \langle\langle \tau_1^{-1} N_1 \rangle\rangle / \langle\langle N_1 \rangle\rangle$; $(\sigma^2 \tau_{A,2}) \equiv \langle\langle \sigma'^2 \tau'_{A,2} N_1 \rangle\rangle / \langle\langle N_1 \rangle\rangle \approx \langle\langle \sigma'^2 N_1 \rangle\rangle \cdot \langle\langle \tau'_{A,2} N_1 \rangle\rangle / \langle\langle N_1 \rangle\rangle^2 \approx \sigma^2 \cdot \tau_{A,2}$; and $(\sigma \tau_{A,2}) \equiv \langle\langle \sigma' \tau'_{A,2} N_1 \rangle\rangle / \langle\langle N_1 \rangle\rangle \approx \sigma \cdot \tau_{A,2}$.
[25] W. Spitzer and H. Y. Fan, Phys. Rev. **108**, 268 (1957).
[26] A. Franceschetti and Y. Zhang, Phys. Rev. Lett. **100**, 136805 (2008).
[27] V. Klimov, A. Mikhailovsky, D. McBranch, C. Leatherdale, and M. Bawendi, Science **287**, 1011 (2000).
[28] F. Trojánek, K. Neudert, M. Bittner, and P. Malý, Phys. Rev. B **72**, 075365 (2005).
[29] J. Heitmann, F. Müller, L. Yi, M. Zacharias, D. Kovalev, and F. Eichhorn, Phys. Rev. B **69**, 195309 (2004).